

DISPATCH methods: an approximate, entropy-based Riemann solver for ideal magnetohydrodynamics

Popovas Andrius^{1,2}

¹ Rosseland Centre for Solar Physics, University of Oslo, P.O. Box 1029, Blindern, NO-0315 Oslo, Norway
e-mail: andrius.popovas@astro.uio.no

² Institute of Theoretical Astrophysics, University of Oslo, P.O. Box 1029, Blindern, NO-0315 Oslo, Norway

Received; accepted

ABSTRACT

Context. With advance of supercomputers we can now afford simulations with very large range of scales. In astrophysical applications, e.g. simulating Solar, stellar and planetary atmospheres, physical quantities, like gas pressure, density, temperature and plasma β can vary by orders of magnitude. This requires a robust solver, which can deal with a very wide range of conditions and be able to maintain hydrostatic equilibrium.

Aims. We reformulate a Godunov-type HLLD Riemann solver so it would be suitable to maintain hydrostatic equilibrium in atmospheric applications and would be able to handle low and high Mach numbers, regimes where kinetic and magnetic energies dominate over thermal energy without any *ad-hoc* corrections.

Methods. We change the solver to use entropy instead of total energy as the 'energy' variable in the system of MHD equations. The entropy is **not conserved**, it increases when kinetic and magnetic energy is converted to heat, as it should.

Results. We conduct a series of standard tests with varying conditions and show that the new formulation for the Godunot type Riemann solver works and is very promising.

Key words. methods: numerical – hydrodynamics– shock waves – magnetohydrodynamics (MHD) – Sun: atmosphere – turbulence

1. Introduction

Turbulent magnetized gas is ubiquitous in astrophysics. In a single system (e.g. stellar and planetary atmospheres, interstellar medium, etc.), the physical quantities, like density, gas pressure, entropy and temperature can vary by orders of magnitude. Let's take our closest star, the Sun, as an example. It has several distinct regions. In the core, energy is generated by nuclear fusion and diffused outward by radiation (gamma and X-rays). Soon the temperature drops sufficiently enough for ions to recombine, which in turn increase the opacity of the plasma and the radiative diffusion can no longer efficiently transport the energy outwards and the plasma starts to 'boil'. Here, the convective zone begins. The transition between the radiative core and the convective zone is rather narrow, on the order of 10 Mm (Elliott & Gough 1999) and is called the tachocline. The convective zone spans roughly 200 Mm and makes up the outer 30% of the solar interior. The energy flux causes the plasma to swirl in turbulent eddies and spirals called convective flows. The convective motions are seen at the solar surface (the photosphere) as granules and supergranules. The convective turnover timescale varies by 4 orders of magnitude - near the tachocline is of the order of 25 – 30 days; and near the photosphere it is approximately 300 seconds. Above the photosphere, in the chromosphere, the thermal energy of the gas no longer dominates the total energy budget, plasma β drops below unity, indicating, that magnetic pressure becomes higher than the gas pressure, and the gas flows must follow the magnetic field configuration. Even higher up, the gas temperature suddenly goes back up to millions degrees Kelvin. The physical quantities, like density, gas pressure, temperature, varies by many orders of magnitude from the deep interior all the

way up to the outermost parts of the Sun. However, in the convective zone, radially averaged entropy per unit mass is nearly constant.

With the advent of exascale computing we are able to run numerical simulations of increasing complexity - either covering larger range of physical and temporal scales, or including more physics, like radiative heat transfer, conductivity, chemistry, non-local thermal equilibrium, generalized Ohm's law, etc. It requires a very flexible solver for the fluid equations of conservation to deal with a large range of physical conditions. The DISPATCH framework (Nordlund et al. 2018) can use several different solvers for magnetohydrodynamics (MHD), we currently use STAGGER-based and Riemann solver groups:

- an internal energy based STAGGER solver taken from the Bifrost (Gudiksen et al. 2011) code, which then was adapted to work well with local timesteps;
- an entropy based STAGGER solver, used in (Popovas et al. 2018, 2019);
- several Godunov-type Riemann solvers:
 - HLL, HLLC and HLLD solvers, based on ones from the public domain RAMSES code (Teyssier 2002; Teyssier et al. 2006; Fromang et al. 2006)
 - Roe solver based on works by Winters & Gassner (2016); Derigs et al. (2016)

Both of these solver groups have their own benefits and limitations. The first, STAGGER group, is good under conditions where magnetic fields are dominating the energy budget, as they were developed with upper Solar atmosphere and corona in mind. On the other hand, they are very diffusive and perform poorly in low Mach number conditions. The Riemann group of

solvers are much better in conditions where detailed turbulent structures ought to be preserved, but due to numerical precision cannot accurately evolve thermal energy, when kinetic and magnetic energies dominate the energy budget – this can create negative pressure spots in e.g. Solar corona, cause inaccurate convective flow velocities, or create areas with negative temperature in a giant molecular cloud simulations. This is a well known problem with HLL and Roe type Riemann solvers. Many attempts have been made to mitigate the issue (e.g. Ismail & Roe 2009; Winters & Gassner 2016; Herbin et al. 2020; Gallice et al. 2022), which do not necessarily resolve the problems, but at least make them negligible under certain conditions.

In this work we present a new approximate entropy-based Riemann solver, which for simplicity here we will call HLLS. It is based on the HLLD solver in RAMSES code (Fromang et al. 2006), also see Miyoshi & Kusano (2005) for a detailed description of a HLLD solver. The HLLS solver is **not entropy conserving** - shocks and magneto-acoustic waves generate entropy by converting kinetic and magnetic energy to heat and this is a fundamental aspect, that must be respected. In a closed system, energy cannot be created or destroyed; it can only change it's form. This is a fundamental requirement and is mathematically¹ fulfilled in total energy-based Riemann solvers. As we are converting the solver to an entropy-based one, we must take into the account the entropy increase in shocks and magneto-acoustic waves. The generated entropy S_{gen} depends on the state of the Riemann fan and is characterised by the change in primitive quantities - density, velocity and total pressure, when crossing a given discontinuity.

In section 2 we will remind the key aspects of the HLLD Riemann solver, as later they will be relevant when discussing the changes and underlying considerations when converting to an entropy-based solver in section 3. If the reader only wants to see the changes, needed to be done for the classical HLLD solver to work with entropy instead of total energy, subsections 3.1 and 3.2 can be skipped and merely used as a reference for notations. The relevant steps are summarized in subsection 3.4. We will show a few numerical tests in section 4. In section 5 we will discuss the current limitations of the solver and the applications, where this solver would be the most beneficial. We will conclude by discussing the future development work.

2. The total energy-based HLLD Riemann solver

The ideal MHD equations are a classical system of equations used to study the dynamics of conducting fluids. In traditional Riemann solvers the fluid equations for the total mass density, momentum density, total energy density and the magnetic field of the system can be written as a system of conservation laws,

$$\frac{\partial}{\partial t} \begin{bmatrix} \rho \\ \rho \mathbf{u} \\ \rho \varepsilon \\ \mathbf{B} \end{bmatrix} + \nabla \cdot \begin{bmatrix} \rho \mathbf{u} \\ \rho(\mathbf{u} \otimes \mathbf{u}) + P_{tot} - \mathbf{B} \otimes \mathbf{B} \\ \mathbf{u}(\varepsilon + P_{tot}) - \mathbf{B}(\mathbf{u} \cdot \mathbf{B}) \\ \mathbf{B} \otimes \mathbf{u} - \mathbf{u} \otimes \mathbf{B} \end{bmatrix} = 0, \quad (1)$$

with

$$\nabla \cdot \mathbf{B} = 0, \quad (2)$$

where ρ , \mathbf{u} , ε , P_{tot} , and \mathbf{B} are density, velocity, total energy, total pressure, and magnetic field respectively. Total energy is a

sum of internal, kinetic and magnetic energies,

$$\varepsilon = E_{int} + \frac{\rho \mathbf{u}^2}{2} + \frac{\mathbf{B}^2}{2}. \quad (3)$$

The system is closed by an equation of state (EOS). In this work, we will limit ourselves to an ideal gas EOS, i.e.

$$P = (\gamma - 1)E_{int} \quad (4)$$

or

$$S = S_0 + \ln(P\rho^{-\gamma}), \quad (5)$$

where S is entropy per unit mass, S_0 is the entropy null-point and γ is the ratio of specific heats (also called adiabatic index). In general, having S_0 is not necessary (i.e. $S_0 = 0$) and mathematically entropy value can be both positive and negative, but physically entropy should not go below 0^2 . Moreover, some slope limiters might get 'confused', thus we keep S always positive for convenience.

The beauty of the system 1 lies in the total energy - when one type of energy is converted to another, one does not have to explicitly compute the conversion via e.g. Maxwell stress tensors, Lorentz force, diagonal Reynolds stress, etc. It saves time and retains very high precision, at least in theory. In practice, however, there are complications, mostly due to numerical floating point precision. If magnetic or kinetic energy strongly dominates over thermal energy, the precision of the latter drops to an extent, that the expressed pressure or temperature can become negative.

3. The conversion to an entropy-based HLLD solver

We use the MUSCL-Hancock algorithm with constrained transport (Evans & Hawley 1988, CT) for the induction equation, as well as a positivity preserving 3D unsplit TVD slope limiter; see Fromang et al. (2006) for details. For convenience, we will not go through the full details of the Godunov scheme and will use standard notation. For deeper overview about HLL, HLLC and HLLD Riemann solvers we recommend looking at excellent works by Miyoshi & Kusano (2005); Toro (2019) and references therein. The main difference from typical HLLD solvers are just the parts where total energy is replaced with entropy.

In the system of equations 1 we replace the total energy term with entropy per unit mass, S :

$$\frac{\partial}{\partial t} \begin{bmatrix} \rho \\ \rho \mathbf{u} \\ \rho S \\ \mathbf{B} \end{bmatrix} + \nabla \cdot \begin{bmatrix} \rho \mathbf{u} \\ \rho(\mathbf{u} \otimes \mathbf{u}) + P_{tot} - \mathbf{B} \otimes \mathbf{B} \\ \rho \mathbf{u} S \\ \mathbf{B} \otimes \mathbf{u} - \mathbf{u} \otimes \mathbf{B} \end{bmatrix} = \begin{bmatrix} 0 \\ -\Phi \\ -\mathbf{Q}/T_{gas} - S_{gen} \\ 0 \end{bmatrix}, \quad (6)$$

where S is entropy per unit mass. For completeness, here we also add the additional source terms, e.g. Φ , force per unit volume, which includes force of gravity, Coriolis force, etc; \mathbf{Q} is heating per unit volume, which includes Newton cooling, radiative heat transfer, etc; T_{gas} is gas temperature and S_{gen} is entropy generation from converting kinetic and magnetic energy to heat. The source terms from gravity, Coriolis forces, Newton cooling, etc. are added during both the predictor and the corrector steps.

² Entropy is usually considered to be either always positive or always negative, or within an interval of $[0, 1]$, with 0 marking the lowest level of disorder. The nomenclature depends on who you ask. We choose to consider entropy being positive.

¹ but not necessarily numerically, as we already know.

The system in 6 can be written in vectorial form, similar to e.g. Londrillo & Del Zanna (2000),

$$\frac{\partial \mathbf{U}}{\partial t} + \frac{\partial \mathbf{F}}{\partial x} + \frac{\partial \mathbf{G}}{\partial y} + \frac{\partial \mathbf{H}}{\partial z} = \Psi, \quad (7)$$

where

$$\mathbf{U} = (\rho, \rho u_x, \rho u_y, \rho u_z, \rho S)^T, \quad (8)$$

$$\Psi = (0, -\Phi_x, -\Phi_y, -\Phi_z, -Q/T_{gas} - S_{gen})^T, \quad (9)$$

and

$$\mathbf{F} = \begin{pmatrix} \rho u_x \\ \rho u_x^2 + P_{tot} - B_x^2 \\ \rho u_x u_y - B_x B_y \\ \rho u_x u_z - B_x B_z \\ \rho u_x S \end{pmatrix} \quad (10)$$

is the flux function. The expressions for the terms \mathbf{G} and \mathbf{H} are completely analogous. These equations have seven eigenvalues, corresponding to four magneto-acoustic (two slow and two fast), two Alfvén waves and an entropy wave:

$$\lambda_{1,7} = u \mp c_f, \quad \lambda_{3,5} = u \mp c_s, \quad \lambda_{2,6} = u \mp c_a, \quad \lambda_4 = u, \quad (11)$$

where

$$c_{f,s}^2 = d \pm \sqrt{d^2 - aB_x^2/\rho}, \quad c_a = \frac{|B_x|}{\sqrt{\rho}} \quad (12)$$

with

$$d = \frac{a^2 + |\mathbf{B}|^2}{2}, \quad (13)$$

and a is the speed of sound. For convenience, similarly to Brio & Wu (1988); Roe & Balsara (1996) we define α_f and α_s parameters, which measure how closely the fast/slow waves approximate the behavior of acoustic waves (Roe & Balsara 1996):

$$\alpha_f^2 = \frac{a^2 - c_s^2}{c_f^2 - c_s^2}, \quad \alpha_s^2 = \frac{c_f^2 - a^2}{c_f^2 - c_s^2}, \quad (14)$$

and they have useful properties, e.g. $\alpha_f^2 + \alpha_s^2 = 1$, $\alpha_f^2 c_f^2 + \alpha_s^2 c_s^2 = a^2$. These α values will become relevant when we will get to the S_{gen} .

More often than not some eigenvalues in 11 coincide,

$$\lambda_1 \leq \lambda_2 \leq \lambda_3 \leq \lambda_4 \leq \lambda_5 \leq \lambda_6, \quad (15)$$

depending on the direction and strength of the magnetic field. A solution to the Riemann problem then may be composed not only of ordinary shock and refraction waves, but also compound waves (Brio & Wu 1988; Miyoshi & Kusano 2005).

3.1. The numerical method

In Godunov-type schemes the volume-averaged conservative physical quantities at a next time-step are given by integrating an approximate solution to the Riemann problem with left and right states, U_L and U_R at the cell interface. An HLL Riemann solver (Harten et al. 1983) is constructed by assuming an average intermediate state between the fastest and slowest waves. The information is lost, as slow magneto-acoustic waves are merged together with Alfvén and entropy waves. An HLLC Toro et al. (1994) solver expands and estimates the middle wave of the contact surface. Lastly, HLLD Miyoshi & Kusano (2005) expands into four intermediate states. We start with computing the HLL wave speed. Usually the wave speeds are notated by S_L and S_R , but to avoid the confusion with entropy, we will note them with Σ_L and Σ_R :

$$\begin{aligned} \Sigma_L &= \min(u_l, u_r) - \max(c_{f,l}, c_{f,r}) \\ \Sigma_R &= \max(u_l, u_r) + \max(c_{f,l}, c_{f,r}) \end{aligned} \quad (16)$$

we define the Lagrangian sound speed,

$$\begin{aligned} v_L &= u_l - \Sigma_L \\ v_R &= \Sigma_R - u_r \end{aligned} \quad (17)$$

and then compute the acoustic star state:

$$u^* = \frac{\rho_r u_r v_R + \rho_l u_l v_L + (P_{tot,l} - P_{tot,r})}{\rho_l v_L + \rho_r v_R} \quad (18)$$

$$P_{tot}^* = \frac{\rho_r v_R P_{tot,r} + \rho_l v_L P_{tot,l} + \rho_r \rho_l v_R v_L (u_r - u_l)}{\rho_l v_L + \rho_r v_R}. \quad (19)$$

The left star region variables are

$$\rho_L^* = -\frac{\rho_l v_L}{\Sigma_L - u^*}, \quad (20)$$

$$v_l^* = \frac{v_l - AB_l(u^* - u_l)}{e_l^*}, \quad (21)$$

$$w_l^* = \frac{w_l - AC_l(u^* - u_l)}{e_l^*}, \quad (22)$$

$$B_l^* = \frac{B_l e_l}{e_l^*}, \quad (23)$$

$$C_l^* = \frac{C_l e_l}{e_l^*}, \quad (24)$$

where v_l and w_l are left tangential velocities, $A = A_l = A_r$ is the normal component of the magnetic field, B_l and C_l are the left states of the tangential components of the magnetic field,

$$e_l^* = -\frac{\rho_l v_L}{\Sigma_L - u^*} - A^2, \quad (25)$$

and

$$e_l = -\frac{\rho_l v_L}{\Sigma_L - u_l} - A^2. \quad (26)$$

Entropy is updated as a passive scalar:

$$S_l^* = \frac{-v_L(S_l - S_0)\rho_l/\rho_l^*}{\Sigma_R - u^*} + S_0. \quad (27)$$

Left state Alfvén wave speed is

$$\Sigma_{a,l} = u^* + \frac{|A|}{\sqrt{\rho_l^*}}. \quad (28)$$

Correspondingly, the right star region variables are:

$$\rho_r^* = -\frac{\rho_r v_r}{\Sigma_R - u^*}, \quad (29)$$

$$v_r^* = \frac{v_r - AB_r(u^* - u_r)}{e_r^*}, \quad (30)$$

$$w_r^* = \frac{w_r - AC_r(u^* - u_r)}{e_r^*}, \quad (31)$$

$$B_r^* = \frac{B_r e_r}{e_r^*}, \quad (32)$$

$$C_r^* = \frac{C_r e_r}{e_r^*}, \quad (33)$$

where v_r and w_r are right tangential velocities, A is the normal component of the magnetic field, B_r and C_r are the tangential components of the magnetic field,

$$e_r^* = -\frac{\rho_r v_R}{\Sigma_R - u^*} - A^2, \quad (34)$$

and

$$e_r = -\frac{\rho_r v_R}{\Sigma_R - u_l} - A^2. \quad (35)$$

$$S_r^* = \frac{-v_R(S_r - S_0)\rho_r/\rho_r^*}{\Sigma_R - u^*} + S_0. \quad (36)$$

Right state Alfvén wave speed is

$$\Sigma_{a,r} = u^* + \frac{|A|}{\sqrt{\rho_r^*}}. \quad (37)$$

Lastly, the double star region variables are:

$$v^{**} = \frac{v_l^* \sqrt{\rho_l^*} + v_r^* \sqrt{\rho_r^*} + \Xi(B_r^* - B_l^*)}{\sqrt{\rho_l^*} + \sqrt{\rho_r^*}}, \quad (38)$$

$$w^{**} = \frac{w_l^* \sqrt{\rho_l^*} + w_r^* \sqrt{\rho_r^*} + \Xi(C_r^* - C_l^*)}{\sqrt{\rho_l^*} + \sqrt{\rho_r^*}}, \quad (39)$$

$$B^{**} = \frac{B_r^* \sqrt{\rho_l^*} + B_l^* \sqrt{\rho_r^*} + \Xi \sqrt{\rho_l^*} \sqrt{\rho_r^*} (v_r^* - v_l^*)}{\sqrt{\rho_l^*} + \sqrt{\rho_r^*}}, \quad (40)$$

$$C^{**} = \frac{C_r^* \sqrt{\rho_l^*} + C_l^* \sqrt{\rho_r^*} + \Xi \sqrt{\rho_l^*} \sqrt{\rho_r^*} (w_r^* - w_l^*)}{\sqrt{\rho_l^*} + \sqrt{\rho_r^*}}, \quad (41)$$

where Ξ is a sign function, $\Xi = \text{sign}(A)$. Note, that there is no double star variable for entropy.

3.2. Godunov fluxes

The fluxes are given by

$$\mathbf{F}_{HLLS} = \begin{cases} \mathbf{F}_L, & \text{if } \Sigma_L > 0 \\ \mathbf{F}_L^*, & \text{if } \Sigma_L \leq 0 \leq \Sigma_{a,l} \\ \mathbf{F}_L^*, & \text{if } \Sigma_{a,l} \leq 0 \text{ and } u^* > 0 \\ \mathbf{F}_R^*, & \text{if } u^* \leq 0 \text{ and } \Sigma_{a,r} > 0 \\ \mathbf{F}_R^*, & \text{if } \Sigma_{a,r} \leq 0 \leq \Sigma_R \\ \mathbf{F}_R, & \text{if } \Sigma_R < 0 \end{cases}, \quad (42)$$

where

$$\mathbf{F}_L = \begin{pmatrix} \rho_l u_l \\ \rho_l u_l^2 + P_{tot,l} - A^2 \\ \rho_l u_l v_l - AB_l \\ \rho_l u_l w_l - AC_l \\ \rho_l u_l S_l \end{pmatrix} \quad (43)$$

$$\mathbf{F}_L^* = \begin{pmatrix} \rho_l^* u^* \\ \rho_l^* u^{*2} + P_{tot}^* - A^2 \\ \rho_l^* u^* v_l^* - AB_l^* \\ \rho_l^* u^* w_l^* - AC_l^* \\ \rho_l^* u^* S_l^* \end{pmatrix} \quad (44)$$

$$\mathbf{F}_L^{**} = \begin{pmatrix} \rho_l^* u^* \\ \rho_l^* u^{*2} + P_{tot}^* - A^2 \\ \rho_l^* u^* v^{**} - AB^{**} \\ \rho_l^* u^* w^{**} - AC^{**} \\ \rho_l^* u^* S_l^* \end{pmatrix} \quad (45)$$

$$\mathbf{F}_R^{**} = \begin{pmatrix} \rho_r^* u^* \\ \rho_r^* u^{*2} + P_{tot}^* - A^2 \\ \rho_r^* u^* v^{**} - AB^{**} \\ \rho_r^* u^* w^{**} - AC^{**} \\ \rho_r^* u^* S_r^* \end{pmatrix} \quad (46)$$

$$\mathbf{F}_R^* = \begin{pmatrix} \rho_r^* u^* \\ \rho_r^* u^{*2} + P_{tot}^* - A^2 \\ \rho_r^* u^* v_r^* - AB_r^* \\ \rho_r^* u^* w_r^* - AC_r^* \\ \rho_r^* u^* S_r^* \end{pmatrix} \quad (47)$$

$$\mathbf{F}_R = \begin{pmatrix} \rho_r u_r \\ \rho_r u_r^2 + P_{tot,r} - A^2 \\ \rho_r u_r v_r - AB_r \\ \rho_r u_r w_r - AC_r \\ \rho_r u_r S_r \end{pmatrix} \quad (48)$$

3.3. Entropy generation

The entropy production in shocks from dissipation of kinetic energy has long been a topic of discussion, as nicely summarized by Salas & Iollo (1995). Such historical figures as Stokes, Kelvin and Rayleigh questioned the validity of shock discontinuity as it violated the conservation of entropy. A very curious result was put forward by Morduchow & Libby (1949), that equilibrium entropy has a maximum inside a Navier-Stokes shock profile, indicating, that entropy was decreasing after passing the shock, strengthening the doubts by Stokes, Kelvin and Rayleigh. Salas & Iollo (1995) explored this curiosity and concluded, that because of this phenomenon, the entropy propagation equation

cannot be used as a conservation law. Using a single jump condition for propagation of entropy is not adequate, as going from equations with two jumps $[P]$ and $[u]$ to an equation with a single jump $[S]$ information is lost. See section 5 in Salas & Iollo (1995) for details. Shocks in the infinitesimally small area cannot be considered equilibrium, as locally the adiabatic index changes because of the rapid compression. Rankine-Hugoniot jump conditions are only applicable when elements are far enough from the discontinuity to assume the local equilibrium is present on each of the both sides, and it is not resolved, what happens in the discontinuity. Margolin (2017) studies non-equilibrium entropy in a shock and shows, that it increases monotonically inside the shock and a certain modification can be done to the equilibrium formulation that it would follow the non-equilibrium formulation better.

Thornber et al. (2008) derives analytical formulae for the rate of increase of entropy at arbitrary jumps in primitive variables for Godunov methods. It is then later used for total energy corrections. We take it a step further and use entropy as the main 'energy' variable. For the main part, the entropy is advected through the Riemann fan as a passive scalar. In addition to that, we compute the increase in entropy when we move along the states of the Riemann fan. We may subdivide the latter part into two closely interconnected components - hydrodynamic and one, influenced by magnetic fields. If no magnetic fields are present, entropy generation between two, L and R states can be written

$$S_{gen} = (u_L - u_R) \left[\ln \left(\frac{P_L}{P_R} \right) + \gamma \ln \left(\frac{\rho_L}{\rho_R} \right) \right]. \quad (49)$$

Shocks and MHD waves interact with each other and readily convert kinetic and magnetic energy into thermal energy. A perfect example of all the wave interactions can be seen in the Solar corona, see e.g. Nakariakov & Verwichte (2005). This must be taken into consideration, thus we expand equation 49 for all the states of the Riemann fan:

$$S_{gen} = \begin{cases} \alpha_{f,l}(u_l - u_r) \left[\ln \left(\frac{P_{tot,l}}{P_{tot,r}} \right) + \gamma \ln \left(\frac{\rho_l}{\rho_r} \right) \right] \\ (u^* - u_r) \left[\ln \left(\frac{P_{tot,l}^*}{P_{tot,r}} \right) + \gamma \ln \left(\frac{\rho_l^*}{\rho_r} \right) \right] \\ (u^* - u_r) \left[\ln \left(\frac{P_{tot,l}^*}{P_{tot,r}} \right) + \gamma \ln \left(\frac{\rho_l^*}{\rho_r} \right) \right] - \xi_L \\ (u_l - u^*) \left[\ln \left(\frac{P_{tot,l}}{P_{tot,l}^*} \right) + \gamma \ln \left(\frac{\rho_l}{\rho_l^*} \right) \right] + \xi_R \\ (u_l - u^*) \left[\ln \left(\frac{P_{tot,l}}{P_{tot,l}^*} \right) + \gamma \ln \left(\frac{\rho_l}{\rho_l^*} \right) \right] \\ \alpha_{f,r}(u_l - u_r) \left[\ln \left(\frac{P_{tot,l}}{P_{tot,r}} \right) + \gamma \ln \left(\frac{\rho_l}{\rho_r} \right) \right] \end{cases}, \quad (50)$$

where

$$\xi_L = \text{sgn}(u_l - u^*) \frac{c_{s,l} \alpha_{s,l} \gamma}{2} \left[\frac{P_l P_{tot,r}}{P_r P_{tot,l}} \right] \quad (51)$$

$$\xi_R = \text{sgn}(u_r - u^*) \frac{c_{s,r} \alpha_{s,r} \gamma}{2} \left[\frac{P_l P_{tot,r}}{P_r P_{tot,l}} \right] \quad (52)$$

and $\text{sgn}()$ is a sign function.

It is clear, that in this formulation S_{gen} can be both positive and negative. But in a closed system entropy can only increase. We note, that S_{gen} is calculated for an interface between two cells and both positive and negative values make perfect sense – the sign indicates, which side of the interface the S_{gen} should be applied to. Positive value indicates positive flow generation, thus the S_{gen} is applied to the right side of the interface, and to the left if the value is negative:

$$s_n^{t+1} = s_n^t + \left(\rho_n^{t+1} \left[\max(0, S_{gen,n-\frac{1}{2}}) - \min(0, S_{gen,n+\frac{1}{2}}) \right] + \frac{Q}{T_{gas}^t} \right) \Delta t,$$

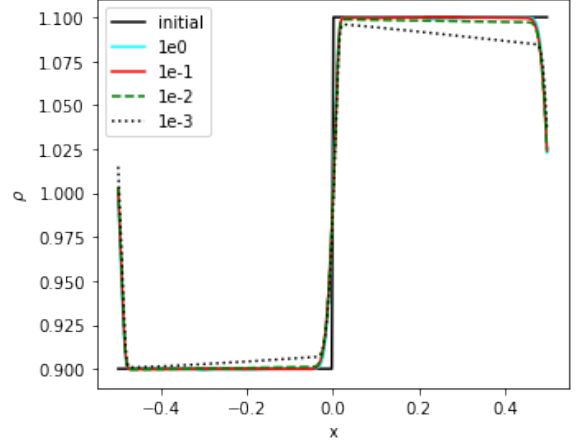


Fig. 1. Entropy wave test. Density profiles at starting time (black) and for different wave speeds u_s : red - 0.1, orange - 0.01, blue - 0.001, green - 0.0001. The overlap of wave profiles is perfect.

(53)

where $s = \rho S$ is entropy per unit volume, t and Δt is time and time-step respectively, Q is heating per unit volume and T_{gas} is the gas temperature.

3.4. Summary

To reformulate a total-energy-based HLLD Riemann solver, we need to replace the total energy with entropy in both predictor and corrector steps, if Godunov method is used. Here are the steps:

1. Replace thermal energy-based EOS 4 with entropy-based EOS 5;
2. For the predictor step, convert S to primitive variable, $s = \rho S$;
3. In the predictor step, it is sufficient to advect S as a passive scalar to get the source term σ , e.g. for the right state:

$$\sigma_s = \frac{\Delta t}{2} \left(-\mathbf{u} \frac{\partial s}{\partial t} \right) \pm \frac{\Delta \xi}{2} \left(-\mathbf{u} \frac{\partial s}{\partial \xi} \right), \quad (54)$$

where $\xi = [x, y, z]$ is the spatial dimension;

4. Compute the Godunov flux for entropy instead of total energy;
5. Compute the S_{gen}
6. Apply Godunov flux, heating and S_{gen} to get S^{t+1} .

In the next section we show a number of tests we have put this new solver through.

4. The numerical tests

To check the validity of the HLLS solver, we conduct a series of experiments. They are in 1D, 2D and 3D, both hydrodynamic and MHD. We run 1D tests in all principal directions, 2D tests in all 3 planes, to make sure the solver is well balanced in all dimensions.

4.1. Entropy wave

Riemann solvers are generally very good at preserving shocks. Very slowly moving waves are, however, sometimes more difficult. To test the diffusion and dispersion error, we launch a

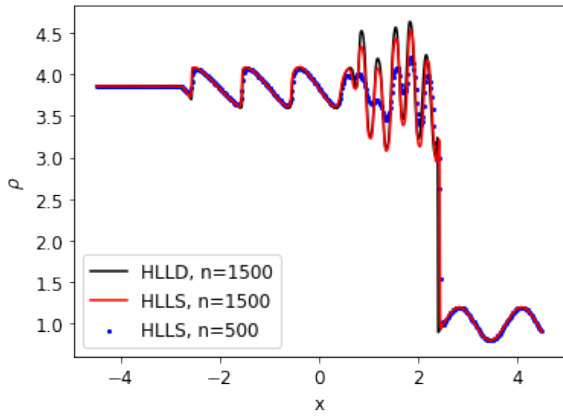


Fig. 2. Shu & Osher shocktube test. Density profile at time=1.8; black - reference HLLD solver with 1500 cells, red - HLLS solver with 1500 cells, blue dots - HLLS solver with 500 cells.

very slowly moving discontinuity (entropy wave) in one dimension. Assuming the experiment is carried out in x direction, the generic quantities are $(\rho, p) = [0.9, 1.0]$ when $x < 0$ and $[1.1, 1.0]$ when $x \geq 0$. All the other quantities are set to 0, with $\gamma = \frac{5}{3}$ and $S = \log(\frac{p}{\rho^\gamma})$ in the whole experiment. The velocity u_x of the whole box is set constant to $[1.0, 0.1, 0.01, 0.001]$ and the runtime of the experiment is set to respectively $t_{end} = [10, 10, 100, 1000]$ time units. This means the number of updates is increasing tenfold with each run. If the solver is diffusive, the wave form should smear out. Figure 1 shows the test results at the end time, when the wave crosses one period. Naturally the corners are slightly diffused, but we can clearly see, that with lower velocities the increase in diffusion is negligible. The diffusion is resolution-sensitive, and depends on the slope limiters. The cyan curve is at time=0, red - $u_x = 0.1$, green - $u_x = 0.01$, blue dotted - at $u_x = 0.001$. For the latter velocity we do already see distortion, stemming from gas turning to incompressible gas at such small Mach numbers and Riemann solvers are normally not good with $M \leq 0.2$.

4.2. Shu & Osher shocktube

This test is a 1D Mach=3 shock interacting with sine waves in density (Shu & Osher 1989). It tests the solver's ability to capture both shocks and small-scale smooth flow. The computational domain is 9 length units long and is split into two regions with different conditions in each of them. Assuming the experiment is carried out in x direction, the quantities are $(\rho, u_x, p) = [3.857143, 2.629369, 10.33333]$ when $x < -4$ and $[1 + 0.2 \sin(5x), 0, 0]$ when $x \geq -4$. All the other quantities are set to 0, with $\gamma = 1.4$ and $S = \log(\frac{p}{\rho^\gamma})$ in the whole experiment. Figure 2 shows the test results at time = 1.8 time units (red curve). The reference run is done with the HLLD solver (black curve, nearly completely covered by the red curve). Both the test and the reference runs had 1500 cells. We additionally show a run with 500 cells (dots).

4.3. Brio & Wu shocktube

This is a classical test of an MHD shocktube, described by Brio & Wu (1988, section V), where the right and left states are initialized to different values. The left state is initialized as $(\rho, u_x, u_y, u_z, B_y, B_z, p) = [1, 0, 0, 1, 0, 1]$, and the right state $[0.125, 0, 0, -1, 0, 0.1]$. $B_x = 0.75$ and $\gamma = 2$. This test shows

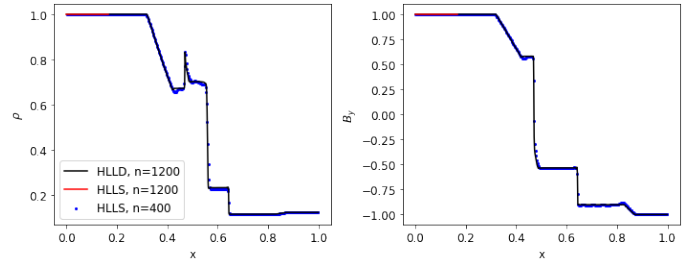


Fig. 3. Brio & Wu shocktube test. Density profile (left) and y component of magnetic field (right) at time=1.0; black - reference HLLD solver with 1200 cells, red - HLLS solver with 1200 cells, blue dots - HLLS solver with 400 cells. Black and red overlap each other nearly perfectly.

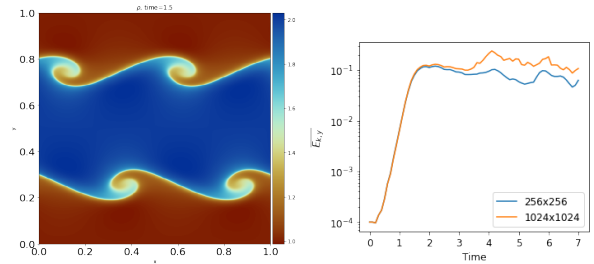


Fig. 4. HD Kelvin-Helmholtz instability. Density profile (left) and time evolution of kinetic energy (right). Density evolution movie available online.

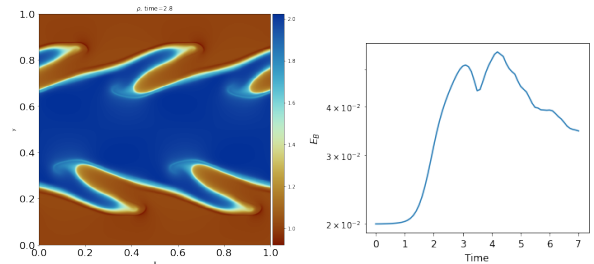


Fig. 5. MHD Kelvin-Helmholtz instability. Density profile (left) and time evolution of magnetic energy (right). Density evolution movie available online.

whether the solver can accurately represent the shocks, rarefaction waves, compound structures and contact discontinuities. Figure 3 shows the test results at time=1.0. Black curve is for reference HLLD run with 1200 cells, red - HLLS run; blue dots - HLLS run with 400 cells. Both high and low resolution runs overlap each other nearly perfectly and follow the profiles in the literature very accurately. From left to right we can identify fast rarefaction fan, compound wave, contact discontinuity, slow shock and a fast rarefaction wave again.

4.4. Kelvin-Helmholtz instability

Kelvin-Helmholtz instability occurs when velocity shear is present within a continuous fluid or across fluid boundaries. We conduct the test as described in McNally et al. (2012). For convenience, here we summarize the setup. The domain is 1 unit by 1 unit in x - and y - directions, with resolutions of 256 x 256

cells. All boundaries are periodic. The density is given by

$$\rho = \begin{cases} \rho_1 - \rho_m e^{-\frac{y-1/4}{L}} & \text{if } 1/4 > y \geq 0 \\ \rho_2 + \rho_m e^{\frac{1/4-y}{L}} & \text{if } 1/2 > y \geq 1/4 \\ \rho_2 + \rho_m e^{-\frac{3/4-y}{L}} & \text{if } 3/4 > y \geq 1/2 \\ \rho_1 - \rho_m e^{-\frac{y-3/4}{L}} & \text{if } 1 > y \geq 3/4 \end{cases}, \quad (55)$$

where $\rho_m = (\rho_1 - \rho_2)/2$, $\rho_1 = 1.0$, $\rho_2 = 2.0$ and $L = 0.025$. The x -direction velocity is given by

$$u_x = \begin{cases} u_1 - u_m e^{-\frac{y-1/4}{L}} & \text{if } 1/4 > y \geq 0 \\ u_2 + u_m e^{\frac{1/4-y}{L}} & \text{if } 1/2 > y \geq 1/4 \\ u_2 + u_m e^{-\frac{3/4-y}{L}} & \text{if } 3/4 > y \geq 1/2 \\ u_1 - u_m e^{-\frac{y-3/4}{L}} & \text{if } 1 > y \geq 3/4 \end{cases}, \quad (56)$$

where $u_m = (u_1 - u_2)/2$, $u_1 = 0.5$ and $u_2 = -0.5$. The background shear is perturbed by adding velocity in y -direction,

$$u_y = 0.01 \sin(4\pi x) \quad (57)$$

An ideal EOS with $\gamma = 5/3$ is used. Initial gas pressure $P_{gas} = 2.5$. We run the simulation until time $t = 10$. To do an exact comparison to codes in McNally et al. (2012), we show the gas density at $t = 1.5$ and the maximal value of vertical kinetic energy evolution in time in figure 4. Note, that we used 256×256 resolution, but our result is directly comparable to 512^2 and 4096^2 runs in McNally et al. (2012). On the right panel of the figure we show the maximum value of vertical kinetic energy in the simulation for three resolutions. From this figure it can be seen, that primary instability sets on at exactly the same time, secondary instabilities occur around the same time as well, indicating that we get a converged solution even at the low resolution of 256×256 .

4.4.1. MHD

Additionally, we have added an ambient magnetic field $B_x = 0.2$. We chose this value for the magnetic field as initially it is weak enough to allow the instability to occur, but later it strengthens enough to suppress it, as can be seen in figure 5, where we show the density at $t = 2.8$, when the instability is starting to be actively suppressed. Magnetic energy peaks at $t = 4.2$ and simulation starts to relax into equilibrium later on.

4.5. Rayleigh-Taylor instability

Another classic test of a code's ability to handle subsonic perturbations is the Rayleigh-Taylor instability and has been described in a number of studies, see e.g. Stone & Gardiner (2007); Abel (2011); Hopkins (2015). In this test a layer of heavier fluid is placed on top of a layer of lighter fluid. With gravitational source term added to the forces we test two things: whether the explicit addition of force is correct and the solver's ability to preserve instabilities while keeping things symmetric where it should be, during the linear phase. During the non-linear phase, in a sufficiently high resolution the symmetry is expected to break by construction. The initial setup we use is similar to Abel (2011); Hopkins (2015). Here we recap the setup for convenience. In two dimensional domain with $0 \leq x \leq 0.5$ (128 cells for low and 768 for high resolution runs) and $0 \leq y \leq 1$ (256 and 1536 cells for low/high resolution runs respectively); we use periodic boundary condition in x direction and constant boundary conditions in y . In this test we use $\gamma = 1.4$ and density profile is initialized as $\rho(y) = \rho_1 + (\rho_2 - \rho_1)/(1 + e^{-(y-0.5)/\Delta})$, where $\rho_1 = 1$ and $\rho_2 = 2$

are the density below and above the contact discontinuity (y_c respectively, with $\Delta = 0.025$ being its width. The pressure gradient is in hydrostatic equilibrium with a uniform gravitational acceleration $g = -0.5$ in the y direction, $P = \rho_2/\gamma + g * \rho(y) * (y - y_c)$, then entropy $S = \ln(P) - \ln(\rho)^\gamma$. An initial y -velocity perturbation $v_y = \delta v_y (1 + \cos(8\pi(x + 0.25)))(1 + \cos(5\pi(y - 0.5)))$ with $\delta v_y = 0.025$ is applied in the range $0.3 \leq y \leq 0.7$ (Hopkins 2015).

Figure 6 shows the evolution of the instability at different times. The initial velocity grows and the heavier fluid starts to sink. Note the single-cell resolution of contact discontinuities and mixing. Both blobs are nearly perfectly symmetric during the linear phase. Soon enough Kelvin-Helmholtz instabilities develop at the shear surface between the fluids and the symmetry is harder to keep, but the low resolution run maintains perfect symmetry throughout the whole simulation. Figure 7 shows the high resolution run. Secondary instabilities are more pronounced and symmetry is harder to maintain. The figure can be directly compared to figure 22 in (Hopkins 2015). Our high resolution (768×1536) run shows very similar features as in (Hopkins 2015), although we maintain much better symmetries until the blobs reach the bottom.

4.6. MHD blast

This is a very popular test and various papers have presented results with slightly different problem setups. It is a very good test of the code ability to handle the evolution of strong MHD waves and look for directional biases. We choose to follow the setup by e.g. Ramsey et al. (2012); Clarke (2010); Stone et al. (2008). We use a rectangular domain with $-0.5 \leq [x, y] \leq 0.5$, 512×512 cells resolution. All boundaries are periodic. $(\rho, u, B_x, B_y, B_z) = (1, 0, 5\sqrt{2}, 5\sqrt{2}, 0)$. The ambient pressure $P_{gas} = 1$ with $P_{gas} = 100$ within radius $r = 0.125$. Figure 8 shows the density and magnetic pressure in the experiment at time $t = 0.021$ and can be directly compared to Ramsey et al. (2012); Clarke (2010); Stone et al. (2008). The shock front is sharp, fast magneto-acoustic wave is traveling at the correct speed, the blast is symmetric.

4.7. Orszag-Tang vortex

This test has become a staple for MHD codes. The initial setup is identical to Stone et al. (2008); Ramsey et al. (2012). We use a rectangular domain with $-0.5 \leq [x, y] \leq 0.5$, 1024×1024 cells for high resolution run. All boundaries are periodic. Initially the pressure and density are constant, $P_{gas} = 5/12\pi$ and $\rho = 25/36\pi$. The ratio of specific heats $\gamma = 5/3$. Initial velocity $(u_x, u_y, u_z) = (-\sin(2\pi y), \sin(2\pi x), 0)$ and the magnetic field is set through the vector potential

$$A_z = \frac{B_0}{4\pi} \cos(4\pi x) + \frac{B_0}{2\pi} \cos(4\pi y),$$

where $B_0 = 1/\sqrt{4\pi}$. In figure 9 we show density, entropy per unit mass and magnetic pressure at two times, $t = 0.5$ and $t = 0.75$. The first time is the typical time this test is shown. When compared to Stone et al. (2008); Ramsey et al. (2012), we can recognize similar features. Notice the very sharp features and perfect symmetry between sides. When advancing the simulation further, the vortex starts producing plasmoids. Here it is very difficult to maintain symmetry, but the lower panels show, that even plasmoids are released symmetrically.

This experiment is great to test the solver stability. In high resolution discontinuities and rarefactions are more severe and

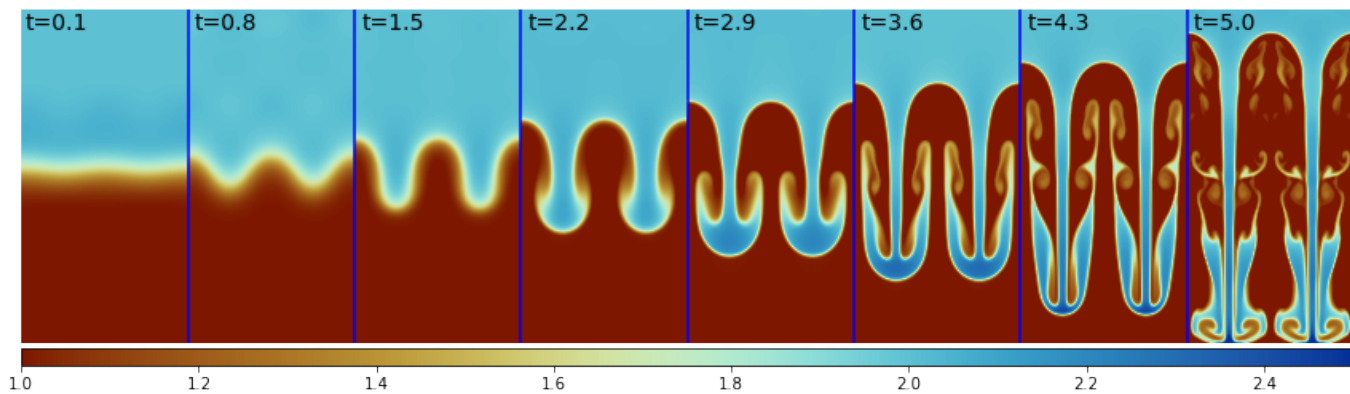


Fig. 6. Rayleigh-Taylor instability in low (128x256) resolution. We plot density at different times.

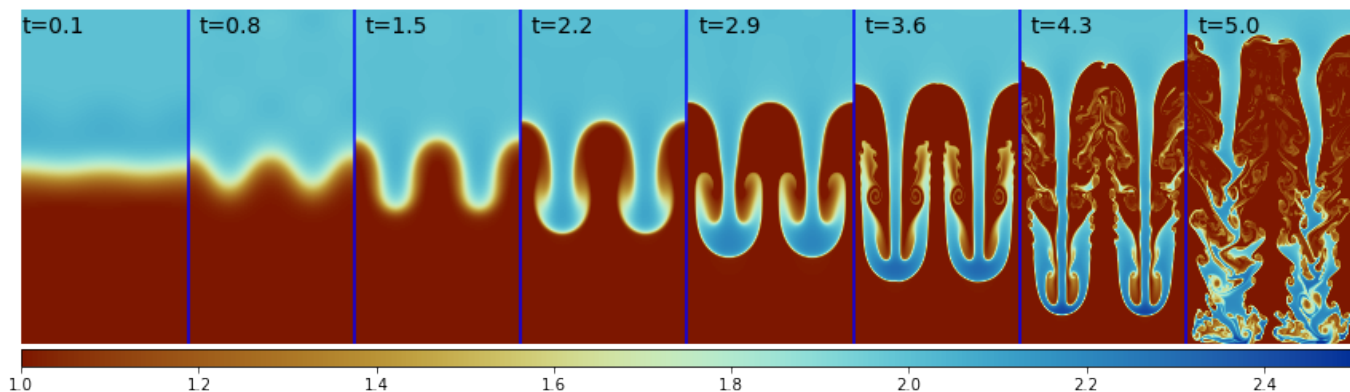


Fig. 7. Same as 6, but in 768x1536 resolution. Movie available online.

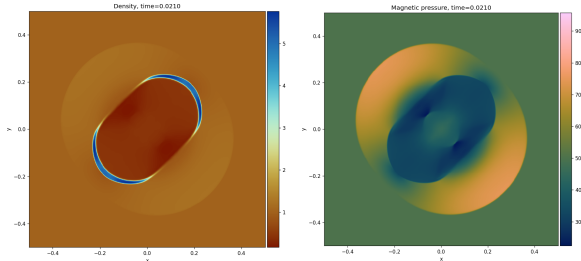


Fig. 8. MHD blast experiment. Density (left) and magnetic pressure (right) at time=0.021. Note the sharp shock-fronts. Movie available online.

Riemann solvers can crash from negative pressure or thermal energy values, if they cannot deal with them. Since we have a HLLD solver available as well, we can see, that the HLLS solver preserves the thermal energy better.

4.8. Current sheet

The current sheet test problem is designed to see what an algorithm will do with a perturbed current sheet. Although an analytic solution for this test problem is not available, it is still a great test to check the robustness of the algorithm. The experimental setup is similar to Hawley & Stone (1995). The test is run in two dimensions using a periodic, square grid with $-0.5 \leq [x, y] \leq 0.5$, 256 x 256 cells resolution. Upon which there is a uniform magnetic field that discontinuously reverses

direction at some point. In the whole box $(\rho, P_{gas}) = (1, \beta/2)$, where β is an input parameter. We set B_y :

$$B_y = \begin{cases} 1/\sqrt{4\pi} & \text{if } |x| > 0.25 \\ -1/\sqrt{4\pi} & \text{if } |x| \leq 0.25 \end{cases}, \quad (58)$$

For $|x| > 0.25$, velocities $(u_x, u_y) = (A \sin(2\pi y), 0)$, where A is an amplitude. We ran the test with a range of β and A values, but here we will show only with the "standard" values, $\beta = A = 0.1$. In figure 10 we show the density and magnetic pressure at different times. Initially linearly polarized Alfvén waves propagate along the field in the y -direction and quickly start generating magneto-acoustic waves since the magnetic pressure does not remain constant. Since there are two current sheets in the setup (at $x = \pm 0.25$, reconnection inevitably occurs. If $\beta < 1$, this reconnection drives strong over-pressurized regions that launch magneto-acoustic waves transverse to the field. Moreover, as reconnection changes the topology of the field lines, magnetic islands form, grow, and merge. The point of the test is to make sure the algorithm can follow this evolution for as long as possible without crashing. We ran tests for $0.1 \leq (\beta, A) \leq 10$ and the HLLS solver deals with it with ease.

4.9. Magnetic field loop advection

This is a very powerful test to check whether the scheme preserves $\nabla \cdot B = 0$. The experiment is similar to Tóth & Odstrčil (1996); Stone et al. (2008) with two dimensional domain, $0 \leq x \leq 2$ (128 cells) and $0 \leq y \leq 1$ (64 cells). We use periodic boundary condition in the whole domain. In this test we use

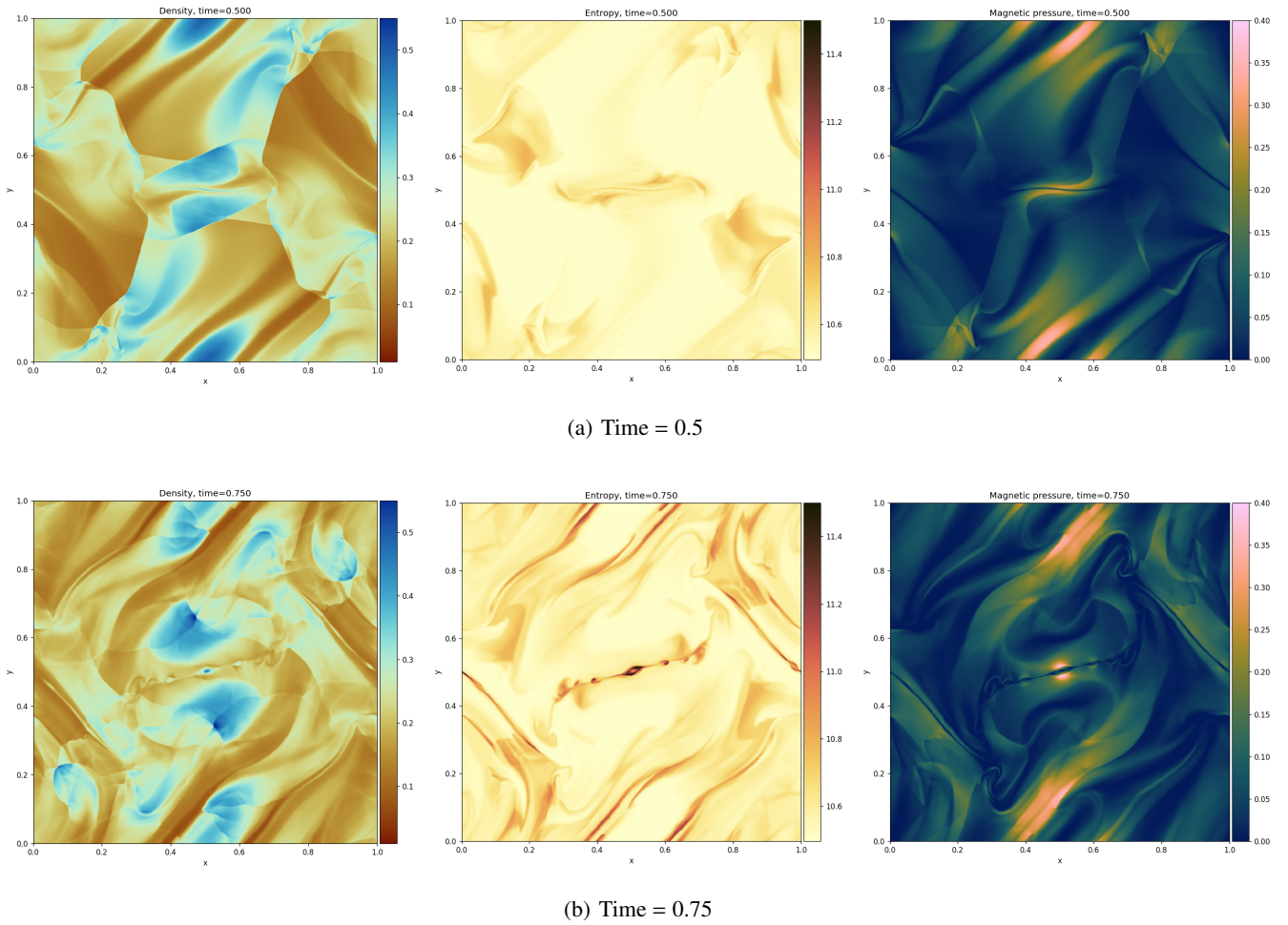


Fig. 9. Orszag-Tang vortex test at two separate times. Density (left), entropy per unit mass (middle) and magnetic pressure (right). Notice the plasmoids forming. Movie available online.

$\gamma = 5/3$ and both density and gas pressure are constant throughout the box, $\rho = P_{gas} = 1.0$. The magnetic field is initialized using a vector potential $A_z = \max[A * (r_0 - r), 0]$, with $A = 10^{-3}$, $r_0 = 0.3$ and r is the radial distance from the domain centre. The flow velocity $(u_x, u_y) = (2, 1)$, thus The problem is essentially an advection test for the vector potential.

Although this test doesn't test the HLLS solver directly, but nonetheless, the CT scheme is an integral part of the solver. Figure 11 shows the initial magnetic pressure and after the magnetic loop has been advected twice through the domain. The shape of the loop is very well preserved.

4.10. Gresho vortex

The Gresho vortex is a time-independent rotation pattern. Angular velocity depends only on the radius and centrifugal force is balanced by the pressure gradient. We use the slightly modified initial condition, which permits the variation of the Mach number, it can be found in Happenhofer et al. (2013); Grimm-Strele et al. (2014). For convenience, we summarize the setup here. The simulation is in two dimensions, $0 \leq x \leq 1$ (48 cells) and $0 \leq y \leq 1$ (48 cells) with periodic boundary conditions everywhere. The low resolution is deliberate - from our tests we see, that with higher resolution (e.g. Grimm-Strele et al. 2014) the experiment becomes much easier. In the whole domain $\rho = 1$,

$\gamma = 5/3$,

$$u_\phi = \begin{cases} 5r & \text{if } 0 \leq r < 0.2 \\ 2 - 5r & \text{if } 0.2 \leq r \leq 0.4 \\ 0 & \text{if } 0.4 < r \end{cases}, \quad (59)$$

$$P_{gas} = \begin{cases} P_0 + \frac{25}{2}r^2 & \text{if } 0 \leq r < 0.2 \\ P_0 + \frac{25}{2}r^2 + 4(1 - 5r - \ln(0.2) + \ln(r)) & \text{if } 0.2 \leq r \leq 0.4 \\ P_0 - 2 + 4 \ln(2) & \text{if } 0.4 < r \end{cases}, \quad (60)$$

where $r = \sqrt{(x^2 + y^2)}$ is the radial distance from the centre of the domain, u_ϕ is the angular velocity in terms of the polar angle $\phi = \text{atan2}(y, x)$ and

$$P_0 = \frac{\rho}{\gamma \text{Ma}_{ref}^2}, \quad (61)$$

with Ma_{ref} being a reference Mach number, which is the highest Mach number in the resulting flow. We execute 5 runs, with $\text{Ma}_{ref} = [0.1, 0.01, 0.001]$. The last Ma_{ref} is repeated in two runs - the nominal resolution and a higher resolution, 128×128 cells. Figure 12 shows the results. We deliberately did not run the experiment with larger Mach numbers, as those are just too easy to maintain. In the figure we can see, that the vortex is maintained very well down to $\text{Ma}=0.01$, and with $\text{Ma}=0.001$ we get

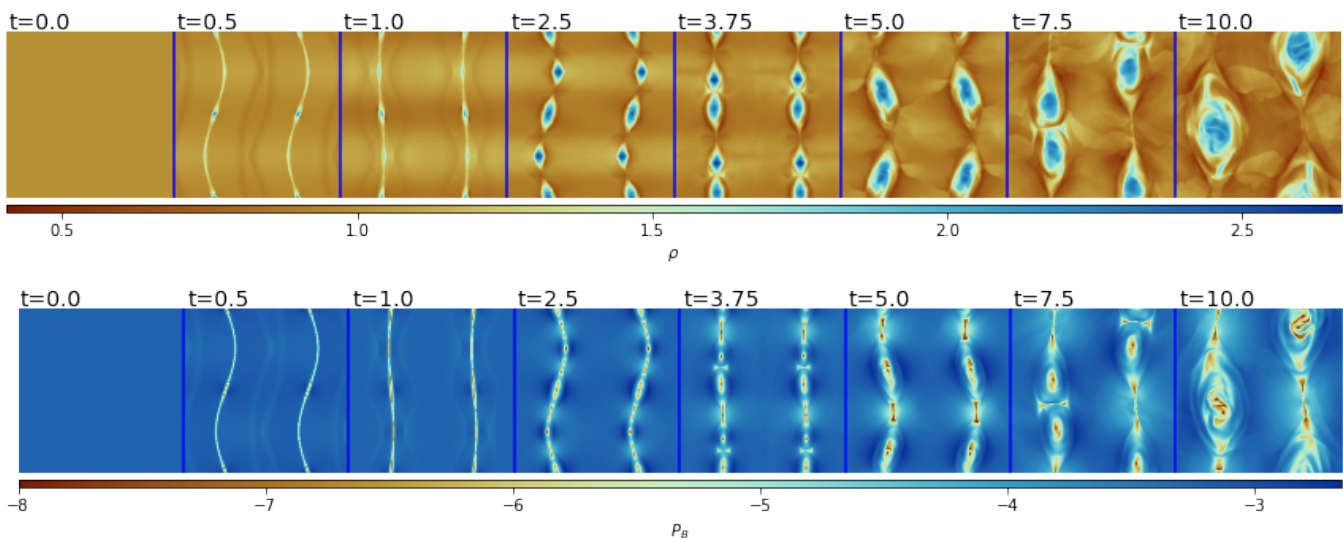


Fig. 10. Current-sheet test at different times. Density (top) and magnetic pressure (bottom). Movie available online.

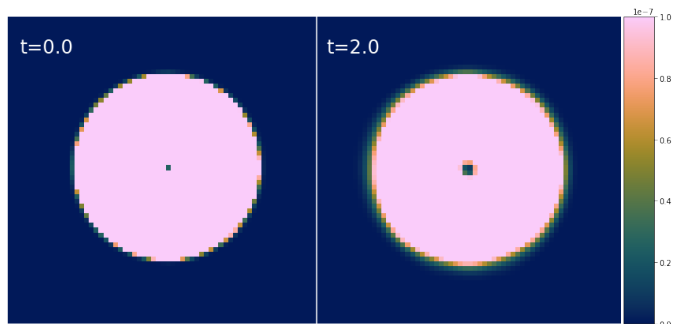


Fig. 11. Magnetic loop advection experiment. The initial magnetic pressure (left) and after the loop has been advected around the grid twice.

the expected outcome - the Godunov type Riemann solvers are not exceptionally great dealing with very low Mach numbers, even though $Ma=0.01$ result is still very good. Especially since we use single floating point precision. Figure 13 shows the gas density and pressure with $Ma=0.01$. It can be clearly seen, that the vortex itself as barely distinguishable inside the noise of the box. On the other hand, with increased resolution, the result with $Ma=0.001$, as expected, has significantly improved and the vortex can be once again identified.

4.11. Magnetic rotor

The magnetic rotor tests the propagation of strong torsional Alfvén waves. A dense disc of fluid rotates within a static fluid background, with a gradual velocity tapering layer between the disc edge and the ambient fluid. An initially uniform magnetic field is present, which is twisted with the disc rotation. The magnetic field is strong enough that as it wraps around the rotor diminishing the rotor’s angular momentum. The increased magnetic pressure around the rotor compresses the fluid in the rotor, giving it an oblong shape. The experimental setup is introduced by Balsara & Spicer (1999) and we use a more stringent variant of it from Guillet et al. (2019), which is summarized below.

The simulation is in two dimensional square, $0 \leq x, y \leq 1$ (512x512 cells) with periodic boundary conditions everywhere. The gas pressure and magnetic fields are uniform in the whole

domain, with $P_{gas} = 1$, $\gamma = 1.4$ and $\mathbf{B} = (5/\sqrt{4\pi}, 0, 0)$. The gas density is

$$\rho = \begin{cases} 10 & \text{if } r < r_0 \\ 1 + 9f & \text{if } r_0 \leq r \leq r_1 \\ 1 & \text{if } r_1 < r \end{cases}, \quad (62)$$

where $r_0 = 0.1$, $r_1 = 0.115$, r is the radial distance from the centre of the box c and $f = (r_1 - r)/(r_1 - r_0)$ is the tapering function for the taper region between the disc and the background. Velocities are

$$(u_x, u_y) = \begin{cases} \left(\frac{v_0(c-y)}{r_0}, \frac{v_0(x-c)}{r_0} \right) & \text{if } r < r_0 \\ \left(f \frac{v_0(c-y)}{r_0}, f \frac{v_0(x-c)}{r_0} \right) & \text{if } r_0 \leq r \leq r_1 \\ (0, 0) & \text{if } r_1 < r \end{cases}, \quad (63)$$

with $v_0 = 2$. The experiment was run until time $t = 0.15$, by which the torsional Alfvén waves have almost reached the boundary. Figure 14 shows the density ρ , magnetic pressure P_B , Mach number and the normalized magnetic field divergence, $\frac{\nabla \cdot \mathbf{B}}{|\mathbf{B}|}$, which, unlike in Guillet et al. (2019), we do not rescale to cell size Δx . We note the very sharp details with no distortions outside the now almond-shaped disc. In the compressed areas the Mach number becomes very high, but it does not pose any issues. The magnetic field is divergence-free within the noise level.

5. Discussion and conclusions

In this work we presented a new approximate entropy-based HLLD Riemann solver. It works well in both sub- and supersonic regimes, preserves positive temperature and gas pressure. The numerical tests are very encouraging and indicate that the HLLS solver can be readily used in a wide range of physical conditions and experimental setups.

5.1. Very low Mach number regimes

Our tests show, that HLLS solver can easily handle Mach numbers to as low as 0.01 and with lower values it becomes rather diffusive. Of course, the perturbations at such Mach numbers are on the order of numerical precision (see Gresho vortex in subsection 4.10 for details) and can be absolutely indistinguishable

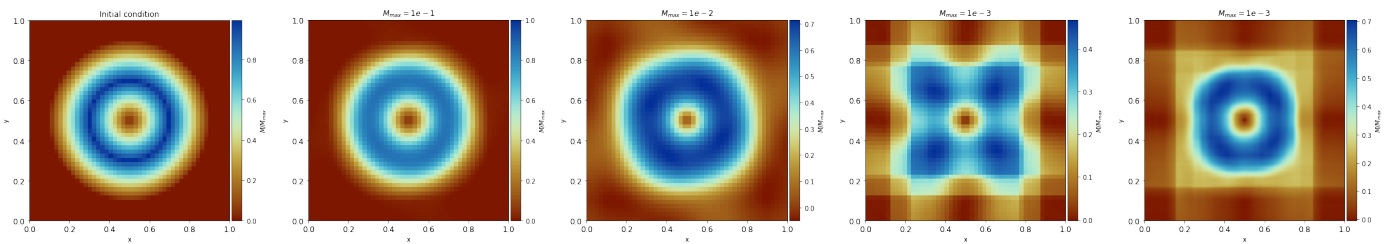


Fig. 12. Gresho vortex test. The initial setup (left) and after 2 rotation periods with different Mach numbers, $Ma = 0.1, 0.01, 0.001$. The rightmost panel is for a higher resolution run. See text for more details.

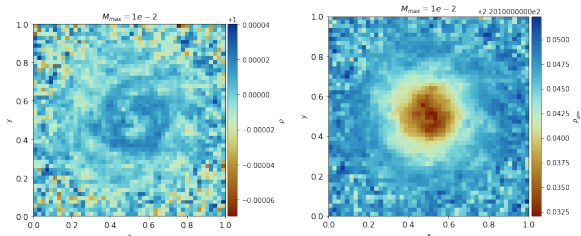


Fig. 13. Gas density (left) and pressure (right) in the Gresho vortex test with $Ma = 0.01$. Note, that the quantities are within the noise limit.

from the background. This is very encouraging, as normally Godunov and Roe type Riemann solvers with single precision struggle with Mach numbers below 0.1. There are different good attempts to modify solvers to go to very low Mach numbers, either adding correction terms into star states, e.g. Shima & Kitamura (2011); Dellacherie et al. (2016); Minoshima & Miyoshi (2021); sheng Chen et al. (2022), or by using well-balanced schemes. In the latter a hydrostatic equilibrium is imposed directly in the set of dynamic equations, separating primitive variables into equilibrium (stationary) states and dynamical perturbations, as it is done in e.g. (Greenberg & Leroux 1996) Hotta et al. (2022); Canivete Cuissa & Teyssier (2022). This approach has less success and not as flexible, as the first option, as although helps with hydrostatic equilibrium in deep atmospheres, numerical precision is better when only perturbations are considered, there is nothing really preventing gas in incompressible state to act as compressible gas and ignore the rotational flows. Our initial attempts to use a simple *ad-hoc* modification to u^* and P_{tot}^* to imitate the transition to incompressible gas at around Mach = 0.2, as in Minoshima & Miyoshi (2021) did not result in any significant improvement and more work has to be done to balance out the equations.

We will continue our work on very low Mach number regimes as this is rather crucial to the applications we intend to use the solver for.

5.2. Applications

The solver was developed with primary intent to use it in the context of Solar, stellar and planetary atmospheres. The from the outermost regions, towards the cores, density, temperature and pressure varies by orders of magnitude, but entropy per unit mass stays almost constant. Additionally, HLLS is the preferred solver in situations where magnetic energy and kinetic energy strongly dominate over thermal energy, e.g. Solar chromosphere and corona.

We are already employing this solver to simulate the whole Solar convective region from 0.655 to 0.995 R_{\odot} Popovas et al. (2022, in prep.) and we can see, that the HLLS solver can main-

tain the hydrostatic equilibrium much better than a HLLD solver without introducing a well-balanced scheme, as in e.g. Canivete Cuissa & Teyssier (2022).

5.3. Future work

In future papers we will discuss the divergence cleaning procedures and the addition of tabular EOS. The latter is needed to do more realistic simulations in astrophysical applications. The HLLS solver requires a slight more care when adding the more general, non-ideal gas EOS. We will keep developing the solver so it would be able to cover a larger range of Mach numbers and in general perform better:

- we intend to implement better slope limiters, e.g. Sekora & Colella (2009);
- solver modifications for very low Mach number regimes;
- solver modifications for relativistic regimes;
- heavy optimization for better memory alignment and vectorization

Acknowledgements. This research was supported by the Research Council of Norway through its Centres of Excellence scheme, project number 262622, and through grants of computing time from the Programme for Supercomputing, as well as through the Synergy Grant number 810218 (ERC-2018-SyG) of the European Research Council.

References

- Abel, T. 2011, Monthly Notices of the Royal Astronomical Society, 413, 271
- Balsara, D. S. & Spicer, D. S. 1999, Journal of Computational Physics, 149, 270
- Brio, M. & Wu, C. 1988, Journal of Computational Physics, 75, 400
- Canivete Cuissa, J. R. & Teyssier, R. 2022, A&A, 664, A24
- Clarke, D. A. 2010, ApJS, 187, 119
- Dellacherie, S., Jung, J., Omnes, P., & Raviart, P.-A. 2016, Mathematical Models and Methods in Applied Sciences, 26, 2525
- Derigs, D., Winters, A. R., Gassner, G. J., & Walch, S. 2016, Journal of Computational Physics, 317, 223
- Elliott, J. R. & Gough, D. O. 1999, ApJ, 516, 475
- Evans, C. R. & Hawley, J. F. 1988, ApJ, 332, 659
- Fromang, S., Hennebelle, P., & Teyssier, R. 2006, A&A, 457, 371
- Gallice, G., Chan, A., Loubère, R., & Maire, P.-H. 2022, Journal of Computational Physics, 468, 111493
- Greenberg, J. M. & Leroux, A. Y. 1996, SIAM Journal on Numerical Analysis, 33, 1
- Grimm-Strele, H., Kupka, F., & Muthsam, H. 2014, Computer Physics Communications, 185, 764
- Gudiksen, B. V., Carlsson, M., Hansteen, V. H., et al. 2011, A&A, 531, A154
- Guillet, T., Pakmor, R., Springel, V., Chandrasekhar, P., & Klingenberg, C. 2019, Monthly Notices of the Royal Astronomical Society, 485, 4209
- Happenhofer, N., Grimm-Strele, H., Kupka, F., Löw-Baselli, B., & Muthsam, H. 2013, Journal of Computational Physics, 236, 96
- Harten, A., Lax, P. D., & Leer, B. V. 1983, SIAM Review, 25, 35
- Hawley, J. F. & Stone, J. M. 1995, Computer Physics Communications, 89, 127, numerical Methods in Astrophysical Hydrodynamics
- Herbin, R., Latché, J.-C., & Zaza, C. 2020, IMA Journal of Numerical Analysis, 40, 1792

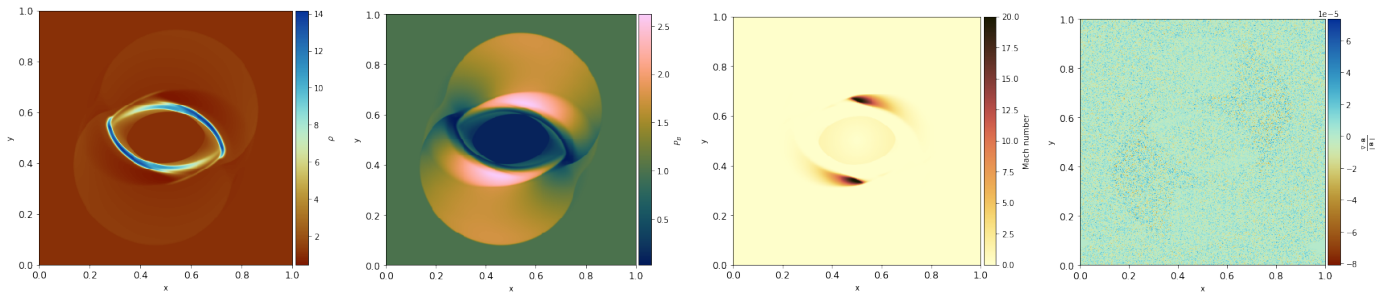


Fig. 14. Magnetic rotor test. From left to right: density, magnetic pressure, Mach number and $\frac{v \cdot B}{|B|^2}$. See text for more details.

- Hopkins, P. F. 2015, *Monthly Notices of the Royal Astronomical Society*, 450, 53
- Hotta, H., Kusano, K., & Shimada, R. 2022, *ApJ*, 933, 199
- Ismail, F. & Roe, P. L. 2009, *Journal of Computational Physics*, 228, 5410
- Londrillo, P. & Del Zanna, L. 2000, *ApJ*, 530, 508
- Margolin, L. 2017, *Entropy*, 19
- McNally, C. P., Lyra, W., & Passy, J.-C. 2012, *ApJS*, 201, 18
- Minoshima, T. & Miyoshi, T. 2021, arXiv e-prints, arXiv:2108.04991
- Miyoshi, T. & Kusano, K. 2005, *Journal of Computational Physics*, 208, 315
- Morduchow, M. & Libby, P. A. 1949, *Journal of the Aeronautical Sciences*, 16, 674
- Nakariakov, V. M. & Verwichte, E. 2005, *Living Reviews in Solar Physics*, 2, 3
- Nordlund, Å., Ramsey, J. P., Popovas, A., & Küffmeier, M. 2018, *MNRAS*, 477, 624
- Popovas, A., Nordlund, Å., & Ramsey, J. P. 2019, *MNRAS*, 482, L107
- Popovas, A., Nordlund, Å., Ramsey, J. P., & Ormel, C. W. 2018, *MNRAS*, 479, 5136
- Popovas, A., Nordlund, Å., & Szydlarski, M. 2022, in prep., *A&A*
- Ramsey, J. P., Clarke, D. A., & Men'shchikov, A. B. 2012, *ApJS*, 199, 13
- Roe, P. L. & Balsara, D. S. 1996, *SIAM Journal on Applied Mathematics*, 56, 57
- Salas, M. D. & Iollo, A. 1995, *Entropy jump across an inviscid shock wave*, Final Report Institute for Computer Applications in Science and Engineering, Hampton, VA.
- Sekora, M. & Colella, P. 2009, arXiv e-prints, arXiv:0903.4200
- sheng Chen, S., ping Li, J., Li, Z., Yuan, W., & hong Gao, Z. 2022, *Journal of Computational Physics*, 456, 111027
- Shima, E. & Kitamura, K. 2011, *AIAA Journal*, 49, 1693
- Shu, C.-W. & Osher, S. 1989, *Journal of Computational Physics*, 83, 32
- Stone, J. M. & Gardiner, T. 2007, *The Astrophysical Journal*, 671, 1726
- Stone, J. M., Gardiner, T. A., Teuben, P., Hawley, J. F., & Simon, J. B. 2008, *The Astrophysical Journal Supplement Series*, 178, 137
- Teyssier, R. 2002, *A&A*, 385, 337
- Teyssier, R., Fromang, S., & Dormy, E. 2006, *Journal of Computational Physics*, 218, 44
- Thornber, B., Drikakis, D., Williams, R. J. R., & Youngs, D. 2008, *Journal of Computational Physics*, 227, 4853
- Toro, E. F. 2019, *Shock Waves*, 29, 1065
- Toro, E. F., Spruce, M., & Speares, W. 1994, *Shock Waves*, 4, 25
- Tóth, G. & Odstrčil, D. 1996, *Journal of Computational Physics*, 128, 82
- Winters, A. R. & Gassner, G. J. 2016, *Journal of Computational Physics*, 304, 72